

## Supporting Information

# High efficient CO<sub>2</sub> electrolysis within a wide operation window using octahedral tin oxide single crystals

*Hai Liu<sup>#,a</sup>, Yaqiong Su<sup>#,b,c</sup>, Siyu Kuang<sup>a</sup>, Emiel J.M. Hensen<sup>b</sup>, Sheng Zhang<sup>\*,a</sup>, Xinbin Ma<sup>\*,a</sup>*

[a] Key Laboratory for Green Chemical Technology of Ministry of Education, Collaborative Innovation Centre of Chemical Science and Engineering, School of Chemical Engineering and Technology, Tianjin University, Tianjin 300072, China. Email: [xbma@tju.edu.cn](mailto:xbma@tju.edu.cn) (ORCID: [0000-0002-2210-0518](https://orcid.org/0000-0002-2210-0518)) [sheng.zhang@tju.edu.cn](mailto:sheng.zhang@tju.edu.cn) (ORCID: [0000-0001-7532-1923](https://orcid.org/0000-0001-7532-1923))

[b] Laboratory of Inorganic Materials and Catalysis, Department of Chemical Engineering and Chemistry, Eindhoven University of Technology, P.O. Box 513, 5600 MB Eindhoven, The Netherlands.

[c] School of Chemistry, Xi'an Key Laboratory of Sustainable Energy Materials Chemistry, MOE Key Laboratory for Nonequilibrium Synthesis and Modulation of Condensed Matter, State Key Laboratory of Electrical Insulation and Power Equipment, Xi'an Jiaotong University, Xi'an 710049, China.

## Experimental Procedures

### Materials preparation

Preparation of SnO<sub>2</sub> catalysts. The SnO<sub>2</sub> nanoparticles exposed with high-energy facets were synthesized by a hydrothermal method and denoted as SnO<sub>2</sub> (111) and SnO<sub>2</sub> (332), respectively. For SnO<sub>2</sub> (111) catalyst, 1 mmol SnCl<sub>4</sub>·5H<sub>2</sub>O (0.35 g, Macklin reagents) and 17 mL 1 M tetramethylammonium hydroxide (TMAH, Macklin reagents) were dispersed in 3 mL absolute ethanol with intense ultrasonication, next the mixture was transferred into a 25 mL Teflon-lined stainless-steel autoclave and kept at 200°C for 12 h. The resulting product was collected and centrifuged at 8000 rpm with water and ethanol for several times. Finally, white catalyst powder was obtained after dried at 90°C for 4 h. For SnO<sub>2</sub> (332) catalyst, SnCl<sub>2</sub>·2H<sub>2</sub>O (Macklin reagents) was used as the tin source. In a typical synthesis procedure, 1 mmol tin precursor and 0.315 g polyvinylpyrrolidone (PVP, K-30, Shanghai Yuanye reagents) were added in a mixture of water and ethanol (6 mL, 1:1 for volume ratio) with intense ultrasonication, and then 0.6 mL HCl was added to adjust the pH value about 0.4. The following procedure was the same as the synthesis for SnO<sub>2</sub> (111). Finally, the SnO<sub>2</sub> (332) sample was calcinated in muffle furnace at 400°C for 2 h to remove the possibly residual substance on catalyst surface. Our XPS spectrum after calcination treatment (see Figure S1d shows no peak of N 1s, demonstrating the absence of PVP. For comparison, spherical SnO<sub>2</sub> (110) NPs was also synthesized using same method as SnO<sub>2</sub> (111) by reducing the amount of TMAH.

### Physical characterizations

The morphology of SnO<sub>2</sub> catalysts were characterized by field-emission scanning electron microscopy (SEM, S-4800) and transmission electron microscopy (TEM, JEOL-2100F and JEOL JEM-ARM200F). The X-ray diffraction (XRD) data were obtained by D8 Advance diffractometer (Bruker) equipped with a Cu K $\alpha$  radiation ( $\lambda=1.5406$  Å, 40 kV, 30 mA) at a scan rate of 8°/min. The surface element compositions of the catalysts were acquired from X-ray photoelectron spectroscopy (XPS) measurements using a photoelectron spectrometer (K-Alpha+) with a monochromatic Al K $\alpha$  X-ray (1486.6 eV) source and all the binding energy was calibrated to C1s signal at 284.8 eV. Electrochemical impedance spectroscopy (EIS) was recorded in Zahner electrochemical station (Zennium Pro) with the frequency of 0.1-10<sup>5</sup> Hz, applied potential of -0.9 V vs. RHE and amplitude of 5 mV.

### *In situ* Raman characterizations

The operando Raman measurements were performed with a confocal Raman microscope (LabRAM HR Evolution, Horiba Jobin Yvon) with a 600 grooves/mm diffraction grating. A laser with 785 nm wavelength was used as the excitation source without attenuation by a filter. The grating was calibrated

before measurements using the first order peak and the Si lattice peak at  $520.7\text{ cm}^{-1}$  of a Si wafer reference sample.

The measurements were conducted in a home-made 3-electrode spectroelectro-chemical cell made from PEEK. Ag/AgCl electrode and Pt wire were used as the reference and counter electrode, respectively. An appropriate amount of suspension of SnO<sub>2</sub> NPs was dropped on an acid-etched Ti foil and it was used as the working electrode. For each experiment, a long working distance objective lens (50 times magnification) was employed and the laser was focused on the catalyst surface. Raman spectra were collected from 400 to 2000  $\text{cm}^{-1}$  and a blank spectrum (Ti substrate) was acquired before the operando experiments (see Figure S9d). The acquisition and accumulation time for each spectrum were 10 s and 5 s, respectively. The spectra were measured from the open circuit potential (OCP) of ca. -0.1 V (after its stabilization) toward cathodic potentials. During each experiment, CO<sub>2</sub> was bubbled through the 0.1 M KHCO<sub>3</sub> electrolyte and the electrolyte was circulated by a peristaltic pump. All the spectra were processed by baseline correction.

#### **Electrochemical active surface area (ECSA) measurement.**

ECSA of the as-prepared catalysts were obtained by double-layer capacitance method, which was described elsewhere from literatures. In this work, cyclic voltammetry (CV) was performed in 0.1 M Ar-saturated KHCO<sub>3</sub> aqueous solution under non-faradaic potential range (-0.6~-0.8 V vs. Ag/AgCl) with different scan rates. Double-layer capacitance ( $C_{dl}$ ) was determined by plotting the  $\Delta J$  ( $\Delta J = J_a - J_c$ ,  $J_a$  and  $J_c$  represent the anodic and cathodic current density, respectively) at -0.7 V vs. Ag/AgCl against the scan rates. Finally, with an assumption that the  $C_{dl}$  of ideal smooth metal oxide surface is  $60\ \mu\text{F cm}^{-2}$ , ECSA can be calculated by following equations:

$$R_f = C_{dl} / 60\ \mu\text{F cm}^{-2}$$

$$ECSA = R_f \times S$$

$R_f$  --- Roughness factor

$S$  --- Geometric area of the working electrode

#### **Electrochemical CO<sub>2</sub> reduction measurements**

The electrochemical experiments were carried out in a custom-made gas-tight H-type cell connected to an electrochemical station (CHI 760E, Shanghai Chenhua). The Ag/AgCl electrode (filled with saturated KCl aqueous solution) and Pt wire was used as the reference electrode and auxiliary electrode, respectively. During the galvanostatic measurement in 3.5 wt. % NaCl, a commercial DSA mesh was used as the anode. A piece of cation exchange membrane (Fumatech) was used as the separator. The glassy carbon electrode (GCE, 6 mm in diameter) with a geometric area of  $0.2826\text{ cm}^2$  was used as the working electrode for all the electrochemical measurements and was pre-polished with Al<sub>2</sub>O<sub>3</sub> powder (0.3 and 0.05  $\mu\text{m}$  in diameter) before each experiment. The as-prepared catalyst samples and 10  $\mu\text{L}$  5wt% Nafion-ethanol solution were dispersed in isopropanol and ultrasonicated for 1 h to form a uniform

catalyst ink with the catalyst concentration of 2 mg·mL<sup>-1</sup>. A calculated amount of carbon black (XC-72) was added to enhance the conductivity and dispersion of the catalysts. A total of 20 μL ink (40 μg catalyst) was dropped on the surface of the pre-polished GCE and last for a few minutes at room temperature to vaporize the solvent. The linear sweep voltammetry was carried out in CO<sub>2</sub>-saturated 0.1 M KHCO<sub>3</sub> electrolyte, while the controlled potential CO<sub>2</sub> reduction was performed in 0.1 M KHCO<sub>3</sub> (or 3.5 wt% NaCl) with a CO<sub>2</sub> flow. All the measured potentials were converted to values versus reversible hydrogen electrode (RHE) according to the following equation:

$$Potential (V \text{ vs. RHE}) = Potential(V \text{ vs. Ag/AgCl}) + 0.197 V + 0.0592 * pH$$

### Products analysis

The gas products (H<sub>2</sub> and CO) were analyzed by an online gas chromatography (GC, Shimadzu 2014 C) equipped with a Porpark-N column and a molecular sieve-5A column, A thermal conductivity detector and a flame ionization detector was used as the detector and high purity Ar (99.999%) was used as the carrier gas. The liquid product (formate) was quantified by high performance liquid chromatography (HPLC, Agilent Technologies) equipped with an Organic Acid-5u column and an ultraviolet detector (UV, 210 nm). 25 mM KH<sub>2</sub>PO<sub>4</sub> aqueous solution (pH=2.5, adjusted by H<sub>3</sub>PO<sub>4</sub>) was used as the mobile phase with the flow rate of 1 mL/min. For each analysis, 50 μL liquid sample was injected and every sample was analyzed at least for three times and the averaged values were reported.

The Cl<sub>2</sub> produced in anolyte when using 3.5 wt. % NaCl was determined by iodometric titration method.<sup>[1]</sup> Briefly, the anolyte after electrolysis was transferred to an iodine flask containing 0.1 g of KI and 0.2 ml of acetic acid. The resulting yellow solution was titrated with 0.01 M Na<sub>2</sub>S<sub>2</sub>O<sub>3</sub> aqueous solution and 1 ml of 0.5 wt. % starch solution was added near the endpoint as the indicator. The Faradaic efficiency of Cl<sub>2</sub> was calculated according to the following formula. Since only the dissolved Cl<sub>2</sub> are detected by the iodometric method, the calculated faradaic efficiency reports a lower limit on the Cl<sub>2</sub> product in the anolyte.

studied herein.

$$FE_{Cl_2} = \frac{2nF}{Q_{total}} \times 100\%$$

n --- the moles of Cl<sub>2</sub> produced in anolyte;

F --- faraday constant, 96485 mol/C;

Q<sub>total</sub> --- the accumulated charge during the galvanostatic measurement.

### Faradaic efficiencies calculation

For the gas products (H<sub>2</sub> and CO),

$$FE_j = \frac{2Fv_0p_0}{RTI_{total}} \times 100\%$$

F --- faraday constant, 96485 mol/C;

$v$  --- volume concentration of the gas products from the electrochemical cell, vol%;

$v_0$  --- gas ( $\text{CO}_2$ ) flow rate at room temperature, calibrated by a mass flowmeter,  $\text{mL min}^{-1}$ ;

$I_{total}$  --- total current measured by electrochemical station, A.

For the liquid product (formate),

$$FE_j = \frac{2FCV}{Q_{total}} \times 100\%$$

C --- concentration of formate in the electrolyte, mol/L;

V --- volume of the electrochemical cell, mL;

$Q_{total}$  --- total charge supplied by the electrochemical station, C.

### Flow cell tests

Flow cell tests were performed in a custom-made reactor made of poly ether ether ketone (PEEK). A  $\text{SnO}_2$ -loaded GDL (SGL-29BC Carbon paper,  $1 \text{ mg}\cdot\text{cm}^{-2}$ ) was used as the working electrode. Ag/AgCl with a diameter of 3.8 mm and a Pt foil was used as the reference and anode electrode, respectively. A piece of cation exchange membrane (Fumatech) was used as the separator. During the tests,  $\text{CO}_2$  was supplied from the back of GDL with a flow rate of 15 sccm controlled by a gas mass flowmeter (Horiba). The catholyte was forced through peristaltic pump to continuously circulate with a flow rate of  $10 \text{ ml}\cdot\text{min}^{-1}$ . The anolyte was circulated by a gas-liquid mixing pump to reduce the disturbance of the produced gas. The applied potential was reported by iR compensation. The Ohmic resistance ( $\sim 1.7 \Omega$ ) was determined by EIS and the resistance was manually compensated.

### DFT calculation details

We carried out spin-polarized calculations within the density functional theory (DFT) framework as implemented in the Vienna *ab initio* simulation package (VASP).<sup>[2]</sup> The ion-electron interactions are represented by the projector-augmented wave (PAW) method<sup>[3]</sup> and the electron exchange-correlation by the generalized gradient approximation (GGA) with the Perdew-Burke-Ernzerhof (PBE) exchange-correlation functional.<sup>[4]</sup> The Kohn-Sham valence states were expanded in a plane-wave basis set with a cut-off energy of 400 eV. The Sn(4p4s), O(2s2p), C(2s2p) and H(1s) electrons were treated as valence states.

For  $\text{SnO}_2$  (111), the models were a periodic ceria slab with a  $(2\times 2)$  surface supercell contains four layers (32 Sn atoms and 64 O atoms), in which the bottom two layers were frozen. For  $\text{SnO}_2$  (110), the models were a periodic ceria slab with a  $(1\times 2)$  surface supercell contains four layers (32 Sn atoms and 64 O atoms), in which the bottom two layers were frozen. For  $\text{SnO}_2$  (332), the models were a periodic ceria slab with a  $(1\times 2)$  surface supercell contains four layers (32 Sn atoms and 64 O atoms), in which the bottom two layers were frozen. The Brillouin-zone integrations were performed using a  $(3\times 3\times 1)$

Monkhorst-Pack mesh during the optimization. The iterative process considered was convergences, when the force on the atom was  $< 0.02 \text{ eV } \text{\AA}^{-1}$  and the energy change was  $< 10^{-5} \text{ eV}$  per atom.

For implicit solvation calculations, we employed VASPsol<sup>[5]</sup> software package that incorporates solvation effect into VASP within a self-consistent continuum model. VASPsol has been generally applied in different electrochemical systems recently due to its simplicity and low computational costs. The energy from DFT is added to the energies from electrostatic interactions between the solute and the solvent and the cavitation energy to create the solute within the solvent. The adopted solvent is water with a dielectric constant of 78.4.

Thermodynamic properties were estimated by means of in-house software Supy. The Gibbs free energies at 298.15 K and 1 atm were calculated with

$$G = H - TS = E_{DFT} + E_{ZPE} + \int_0^{298.15K} C_V dT - TS \quad (1)$$

where  $E_{DFT}$  is the total energy obtained from DFT optimization,  $E_{ZPE}$  is the zero-point vibrational energy using the harmonic approximation,<sup>[6]</sup>  $C_V$  is the heat capacity,  $T$  is the kelvin temperature, and  $S$  is the entropy. The computational hydrogen electrode (CHE) model<sup>[7]</sup> was used to calculate the free energy of electro-catalytic OERs.

The adsorption energy of intermediates was calculated taking the energies of species,  $\text{H}_2$ ,  $\text{HCOOH}$  and clean  $\text{SnO}_2$  facets as reference shown below:

$$E_{\text{ads}}(\text{HCOOH}) = E(\text{facet- HCOOH}) - E(\text{facet}) - E(\text{HCOOH})$$

$$E_{\text{ads}}(\text{OCHO}^*) = E(\text{facet- OCHO}^*) - E(\text{facet}) - E(\text{CO}_2) - 1/2E(\text{H}_2) \text{ for OCHO}^*$$

where  $E(\text{species})$ ,  $E(\text{facet})$ ,  $E(\text{facet-species})$  are electronic energies of free species (species =  $\text{H}_2$  and  $\text{HCOOH}$ ), clean  $\text{SnO}_2$  supports and the species-adsorbed  $\text{SnO}_2$  facets, respectively

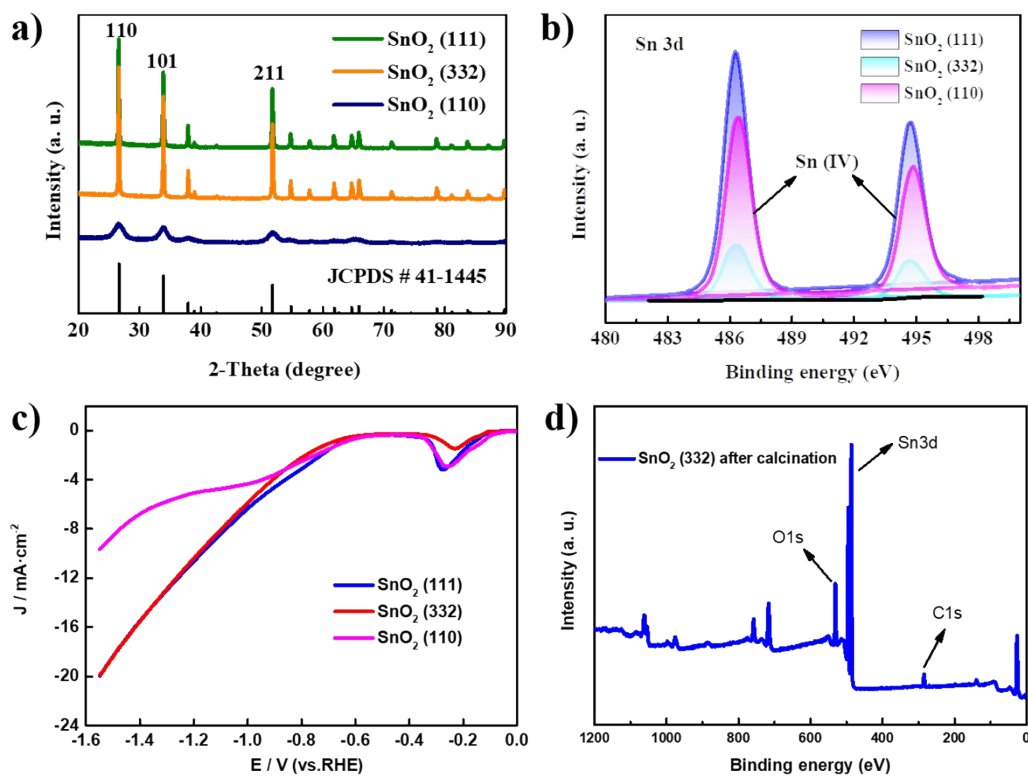


**Figure S1.** (a) XRD, (b) High-resolution Sn 3d XPS spectra and (c) Cathodic LSV results of the as-synthesized SnO<sub>2</sub> catalysts in 0.1 M CO<sub>2</sub>-saturated KHCO<sub>3</sub> electrolyte; (d) XPS spectrum of SnO<sub>2</sub> (332) after calcination.

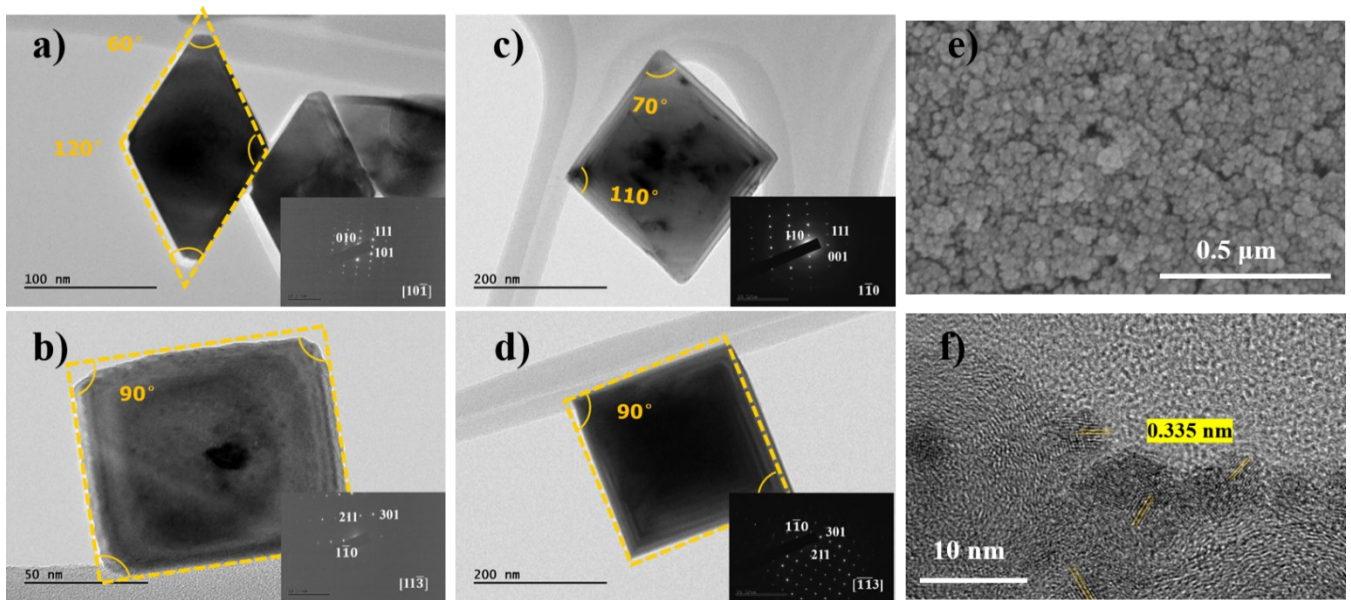


**Figure S2.** (a-d) TEM micrographs and corresponding SAED patterns of SnO<sub>2</sub> (111) and SnO<sub>2</sub> (332); (e-f) SEM and TEM micrographs of SnO<sub>2</sub> (110).

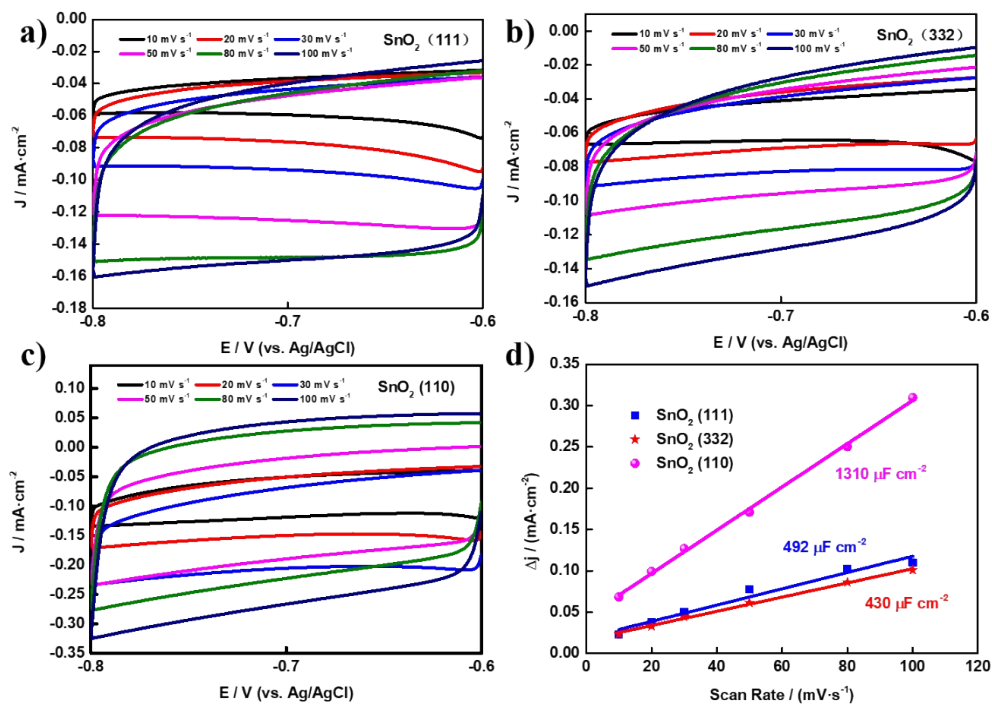


**Figure S3.** (a-c) Cyclic voltammograms (CVs) of SnO<sub>2</sub> (111), SnO<sub>2</sub> (332) and SnO<sub>2</sub> (110) from -0.6~ -0.8 V vs. Ag/AgCl in 0.1 M Ar-saturated KHCO<sub>3</sub>; (d) Charging  $j$  differences ( $\Delta j$ ) plotted against scan rates.

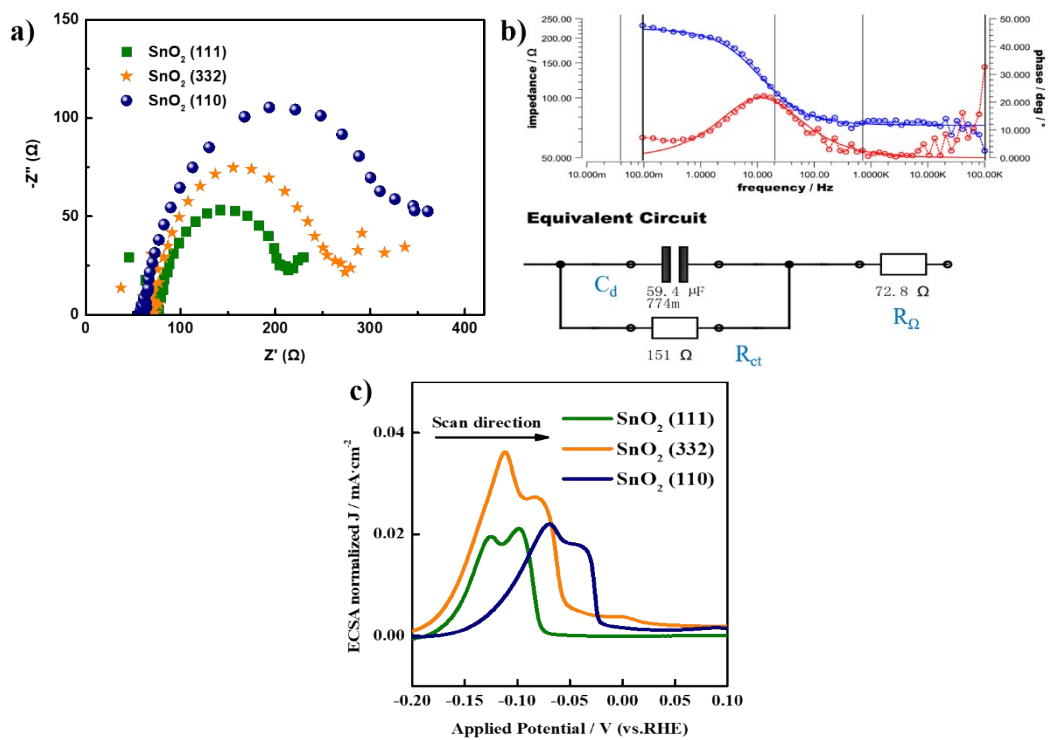


**Figure S4.** Nyquist plots for  $\text{SnO}_2$  (111),  $\text{SnO}_2$  (332) and  $\text{SnO}_2$  (110) (a) and corresponding simulation model (b); (c) ECSA-normalized single oxidative LSV scans at  $50 \text{ mV s}^{-1}$  in Ar-saturated  $0.1 \text{ M KOH}$ .

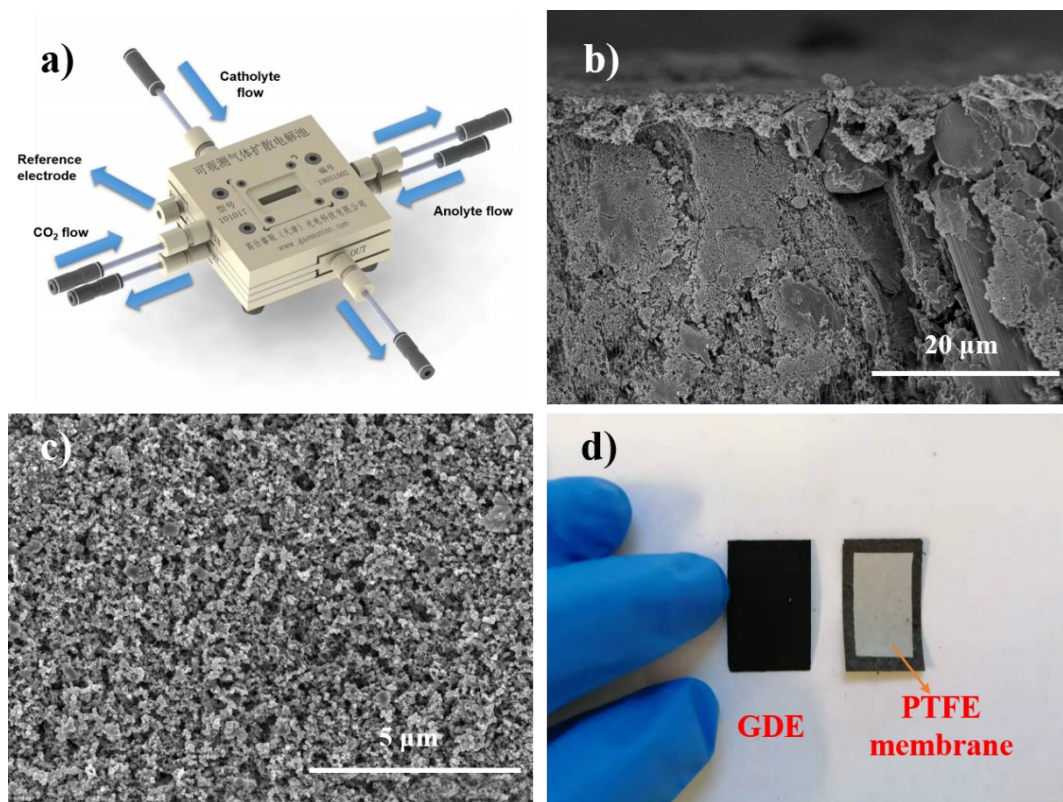


**Figure S5.** (a) Flow cell set-up diagram. GDE configuration with a catalyst layer: (b) cross section and (c) surface; (d) GDE with a PTFE porous hydrophobic layer

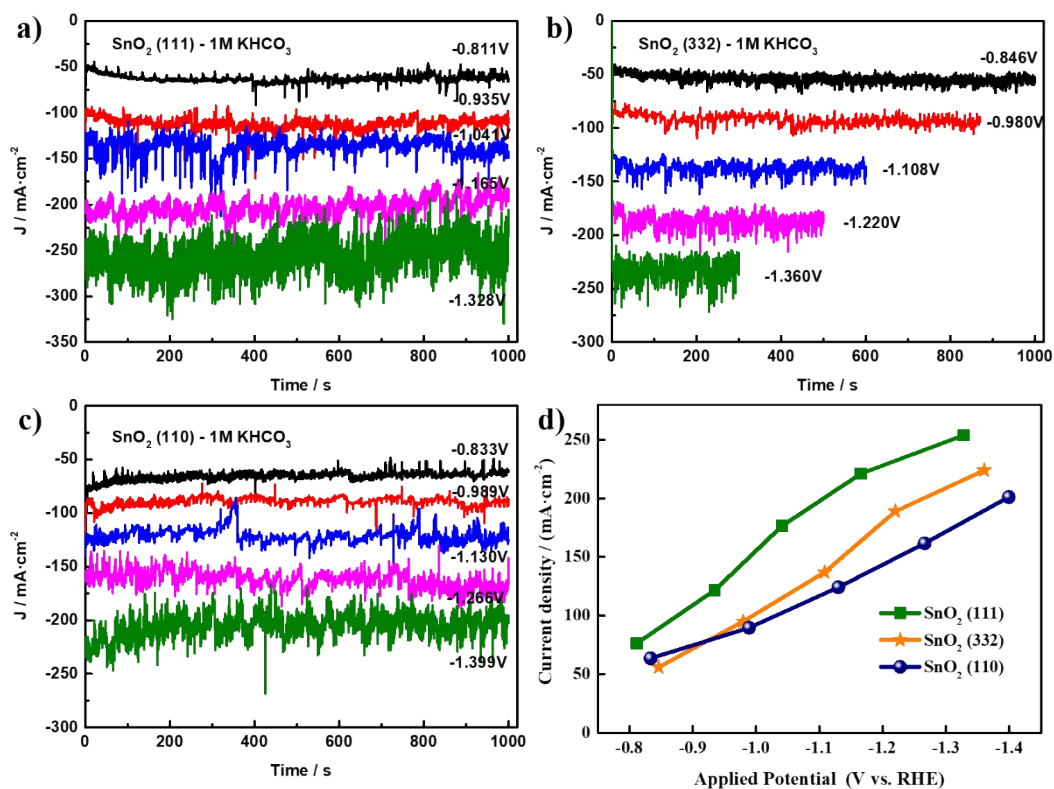


**Figure S6.** Flow cell test results of SnO<sub>2</sub> (111) (a), SnO<sub>2</sub> (332) (b) and SnO<sub>2</sub> (110) (c) at various applied potential and potential-dependent current densities (d) in 1 M KHCO<sub>3</sub>.

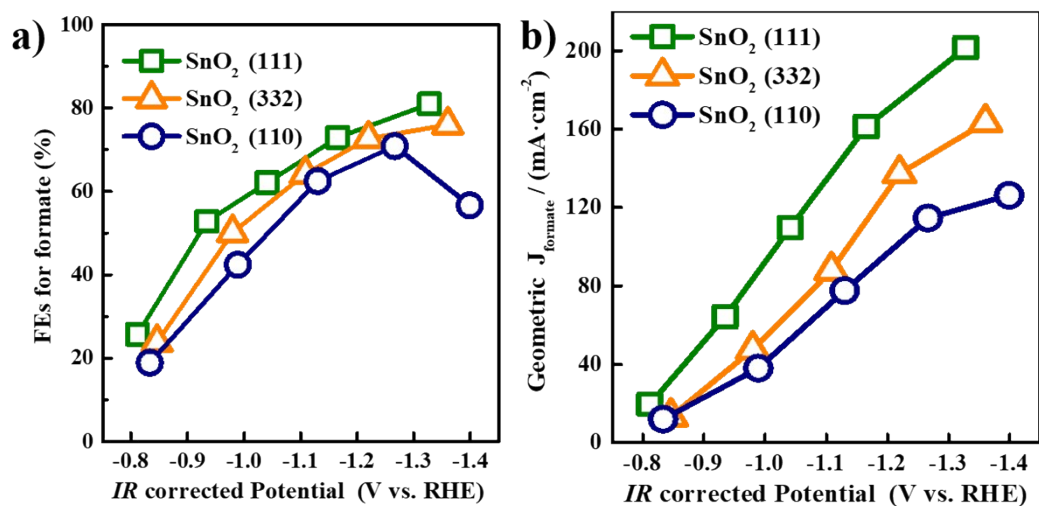


**Figure S7.** Faradaic efficiencies of formate (a) and geometric formate partial current density ( $J_{\text{formate}}$ ) (d) at various IR-corrected potentials in 1 M KHCO<sub>3</sub> in flow cell.

The potential-depended formate Faradaic efficiencies are shown in Figure S7a. Octahedral SnO<sub>2</sub> sample with high-energy facets exhibit higher formate selectivity at lower overpotential than SnO<sub>2</sub> (110), which can be attributed to the intrinsic activity of catalysts and is also consistent with the results in the H-cell. More importantly, as shown in Figure S7b, SnO<sub>2</sub> (111) gives much larger formate partial current density of  $\sim 200 \text{ mA}\cdot\text{cm}^{-2}$  at about -1.3 V vs. RHE in flow cell which is about 20 folds in the H-cell that under the same operation condition.

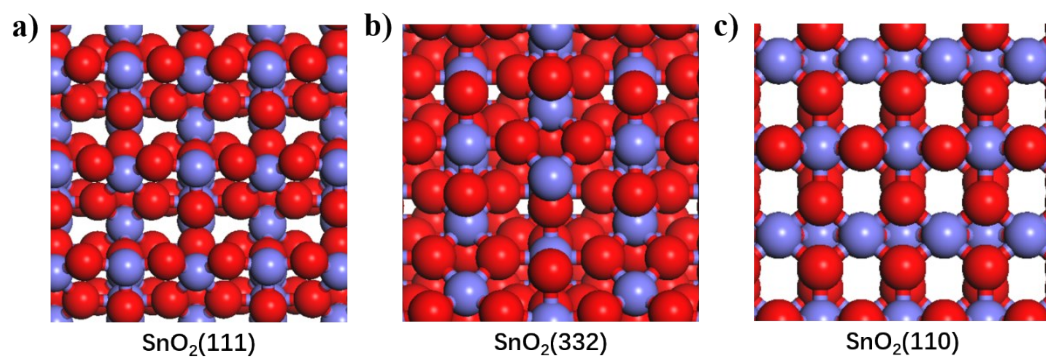


**Figure S8.** Models of the investigated SnO<sub>2</sub> facets. Color code: blue, Sn; red, O.

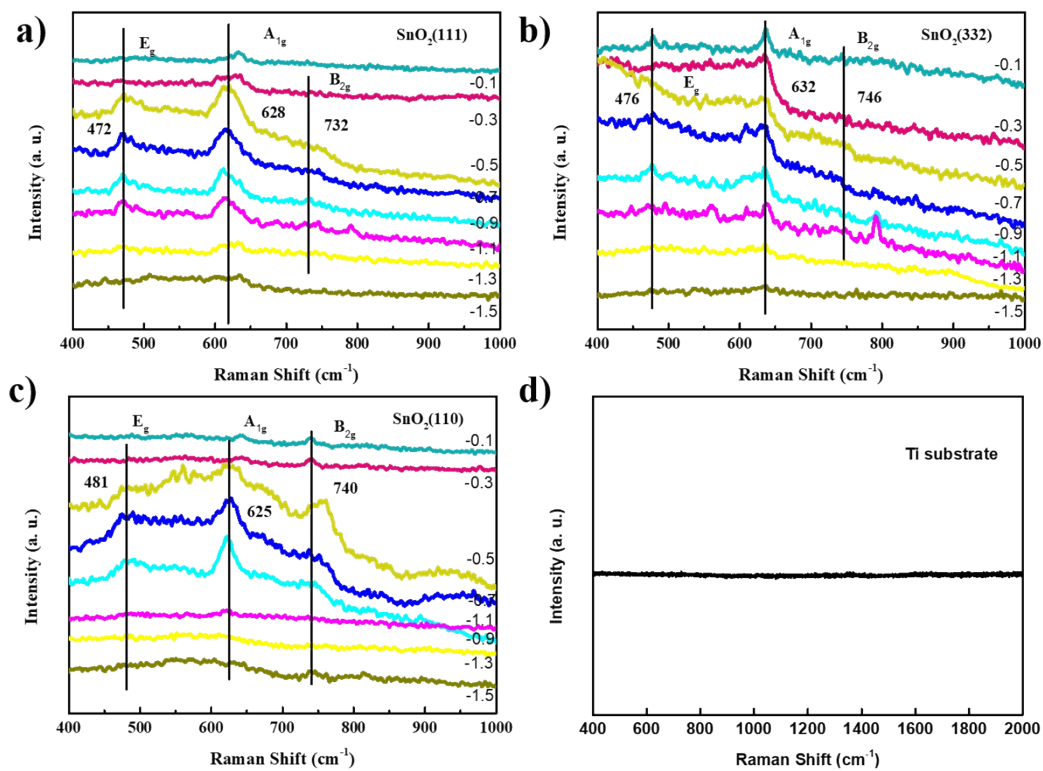


**Figure S9.** (a-c) Electrochemical *in situ* Raman spectra (in the low wavenumber region) on tin oxide samples at various applied potential; (d) Blank Raman spectrum without catalyst.

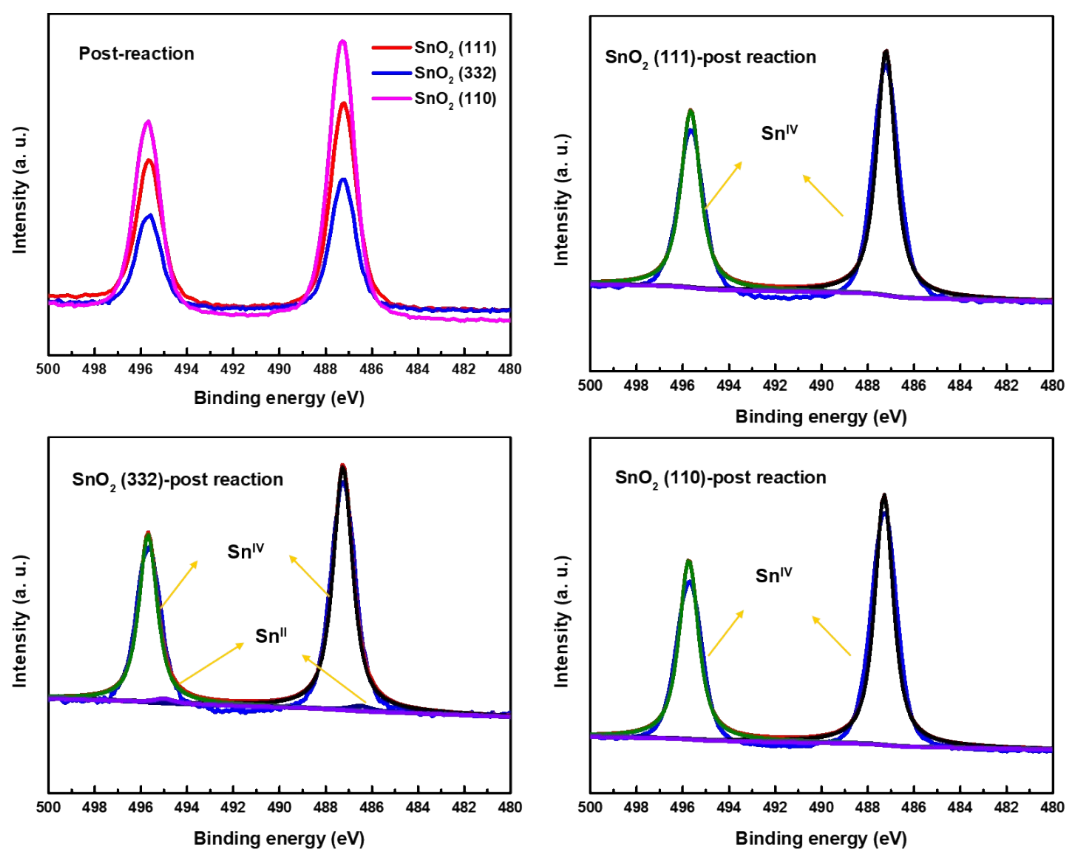


**Figure S10.** High-resolution Sn 3d XPS spectra of SnO<sub>2</sub> (111), SnO<sub>2</sub> (332) and SnO<sub>2</sub> (110) after CO<sub>2</sub> reduction

The SnO<sub>2</sub> catalysts with different facets were electrolyzed at -1.2 V vs. RHE in CO<sub>2</sub>-saturated 0.1 M KHCO<sub>3</sub> for 2h. Next, the samples after electrolysis were collected immediately and characterized by XPS. The high-resolution Sn 3d spectroscopy was shown in Figure S10. As can be observed, there still exist Sn (IV) peaks.

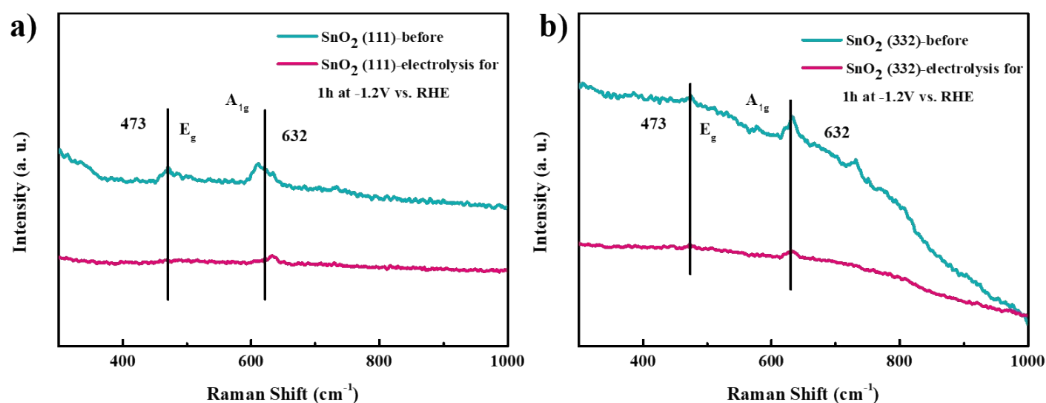


**Figure S11.** Electrochemical *in situ* Raman spectra (in the low wavenumber region) on SnO<sub>2</sub> (111) (a) and SnO<sub>2</sub> (332) before and after CO<sub>2</sub> reduction.

Taking into account of the possible effect of air during handling XPS samples, we conducted electrochemical Raman experiments to *in-situ* monitor the oxidation state of Sn. In this procedure, we firstly collected the Raman spectra of SnO<sub>2</sub> in spectroelectro-chemical cell filled with CO<sub>2</sub>-saturated 0.1 M KHCO<sub>3</sub> electrolyte. Then the CO<sub>2</sub> electrolysis was performed at -1.2 V vs. RHE for 1 h. Finally, *in situ* Raman spectrum was collected again in spectroelectro-chemical cell. The Raman spectra of SnO<sub>2</sub> before and post reaction were presented in SI. As shown in the figure, the characteristic peaks of SnO<sub>2</sub> became weak but still existed even under such harsh reduction potential.

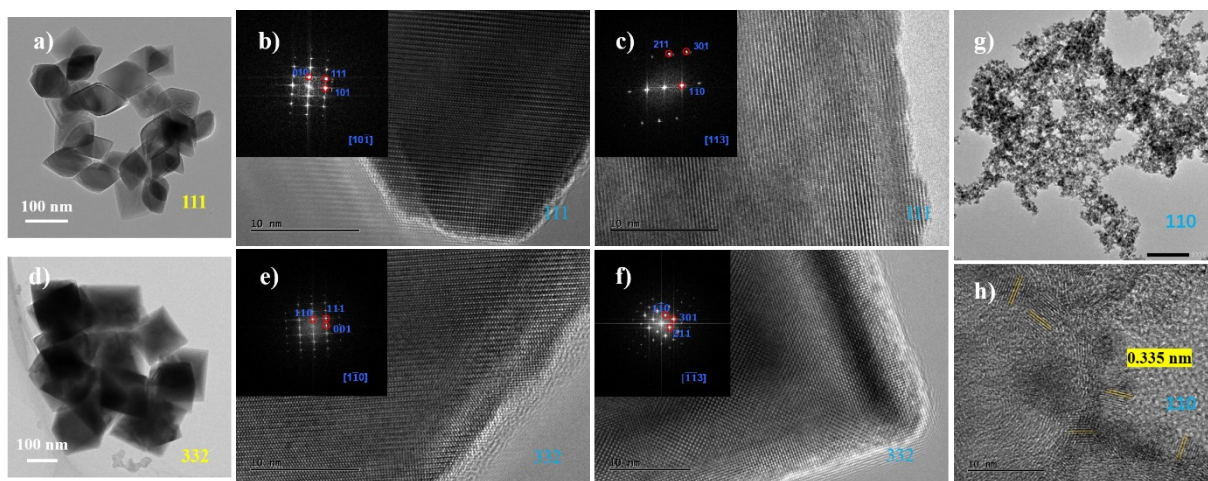


**Figure S12.** TEM micrographs and corresponding FFT patterns of SnO<sub>2</sub> (111) (a-c), SnO<sub>2</sub> (332) (d-f) and SnO<sub>2</sub> (110) (g-h) after CO<sub>2</sub> reduction.

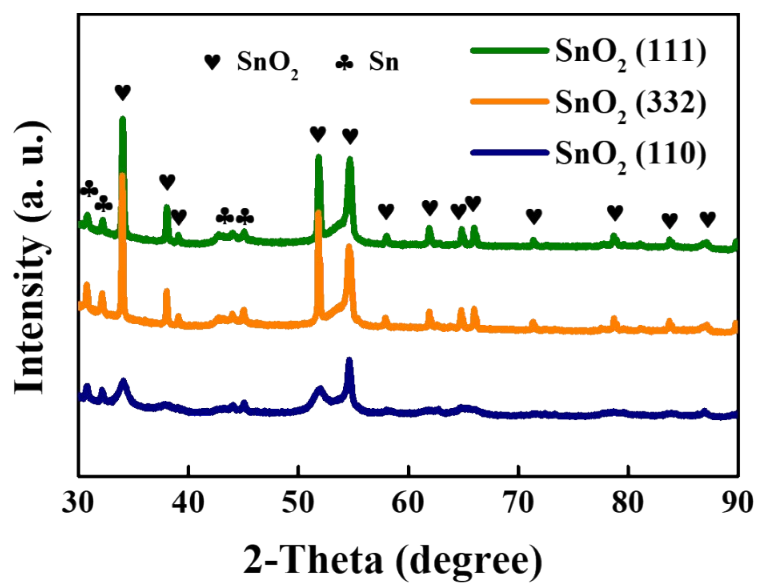


Figure S13. XRD pattern after CO<sub>2</sub> reduction.

**Table S1.**  $C_{dl}$  and ECSA for different SnO<sub>2</sub> NPs.

<b>Catalyst Type</b>	<b><math>C_{dl}/(\mu\text{F}\cdot\text{cm}^{-2})</math></b>	<b>ECSA/ <math>\text{cm}^2</math></b>
SnO <sub>2</sub> (111)	492	2.32
SnO <sub>2</sub> (332)	430	2.02
SnO <sub>2</sub> (110)	1310	6.17

**Table S2.** Equivalent circuit simulation results.

<b>Catalyst Type</b>	<b><math>R_{ct}/\Omega</math></b>	<b><math>R_{\Omega}/\Omega</math></b>
SnO <sub>2</sub> (111)	151	72.8
SnO <sub>2</sub> (332)	205	67.2
SnO <sub>2</sub> (110)	283	96.3

**Table S3.** Predicted Gibbs free energy profiles of CO<sub>2</sub> reduction over various SnO<sub>2</sub> facets, respectively, including the solvent effect.

Species	E (eV)	TS (eV) 298.15K	ZPE (eV)	CvT (eV)	G (eV)
CO <sub>2</sub> (g)	-23.13	0.66	0.31	0.058	-23.43
H <sub>2</sub> (g)	-6.67	0.40	0.30	0.037	-6.73
HCOOH(l)	-30.28	0.44	0.89	0.079	-29.75
CO(g)	-14.83	0.61	0.14	0.047	-15.26
<b>SnO<sub>2</sub>(110)</b>					
* + CO <sub>2</sub> (g)	-608.13				-608.13
CO <sub>2</sub> *	-631.50	0.17	0.32	0.073	-631.27
HCOO*	-634.30	0.26	0.64	0.13	-633.79
HCOOH*	-639.27	0.24	1.00	0.13	-638.37
COOH*	-633.24	0.26	0.65	0.13	-632.71
CO*	-623.34	0.19	0.18	0.090	-623.26
<b>SnO<sub>2</sub>(111)</b>					
* + CO <sub>2</sub> (g)	-587.41				-587.41
CO <sub>2</sub> *	-610.68	0.21	0.31	0.078	-610.49
HCOO*	-614.82	0.15	0.65	0.087	-614.24
HCOOH*	-617.90	0.17	0.90	0.073	-617.09
COOH*	-614.39	0.28	0.66	0.14	-613.87
CO*	-602.33	0.13	0.15	0.059	-602.25
<b>SnO<sub>2</sub>(332)</b>					
* + CO <sub>2</sub> (g)	-601.66				-601.66
CO <sub>2</sub> *	-624.86	0.22	0.32	0.093	-624.67
HCOO*	-628.49	0.29	0.63	0.14	-628.01
HCOOH*	-632.068	0.19	0.90	0.077	-631.28
COOH*	-627.27	0.32	0.67	0.15	-626.77
CO*	-616.58	0.095	0.14	0.041	-616.49

**Table S4** Comparison of the electrocatalytic performance for electroreduction CO<sub>2</sub> to formate over various Sn-based catalysts and electrolytes.

Catalysts	Electrolyte	Applied Potential (V)	$j_{\text{formate}}$ (mA cm <sup>-2</sup> )	FE <sub>formate</sub> (%)	Ref.
Ag <sub>3</sub> Sn@SnO <sub>2</sub>	0.5 M NaHCO <sub>3</sub>	-0.8 V vs. RHE	~16	~80	Feng Jiao et al. <sup>[8]</sup>
Sn/ SnO <sub>x</sub>	0.5 M NaHCO <sub>3</sub>	-0.7 V vs. RHE	0.76	~38	Kanan et al. <sup>[9]</sup>
Sn dendrite	0.1 M KHCO <sub>3</sub>	-1.36 V vs. RHE	12.24	71.6	Seong Ihl Woo et al. <sup>[10]</sup>
SnO NPs	0.5 M KHCO <sub>3</sub>	-0.85 V vs. RHE	~20	69	Xile Hu et al. <sup>[11]</sup>
1D Wire-in-Tube SnO <sub>2</sub>	0.1 M KHCO <sub>3</sub>	-1.29 V vs. RHE	~8.4	~70	Yingying Lu et al. <sup>[12]</sup>
Sn <sub>56.3</sub> Pb <sub>43.7</sub> alloy	0.5 M KHCO <sub>3</sub>	-2 V vs. Ag/AgCl	36.47	79.8	Ki Tae Park et al. <sup>[13]</sup>
Sn-OH-5.9 branches	0.1 M KCl	-1.6 V vs. Ag/AgCl	~9.5	82	Jinlong Gong et al. <sup>[14]</sup>
Single atom Sn <sup>δ+</sup> /N-doped graphene	0.25 M KHCO <sub>3</sub>	-1.62 V vs. SCE	8.8	75.1	Yi Xie et al. <sup>[15]</sup>
Sub-2 nm SnO <sub>2</sub> QWs	0.1 M KHCO <sub>3</sub>	-1.16 V vs. RHE	~12	87.4	Xiongwen Lou et al. <sup>[16]</sup>
Pd-Sn alloy (1:1) NPs/C	0.5 M KHCO <sub>3</sub>	-0.43 V vs. RHE	~1.98	99	Wei Chen et al. <sup>[17]</sup>
Porous SnO <sub>2</sub> /carbon cloth	0.5 M NaHCO <sub>3</sub>	-1.6 V vs. Ag/AgCl	43.2	89	Douglas R. MacFarlane et al. <sup>[18]</sup>
Sn quantum sheets / graphene	0.1 M NaHCO <sub>3</sub>	-1.8 V vs. SCE	17.9	85	Yi Xie et al. <sup>[19]</sup>
Sn/SnO <sub>2</sub> hollow fiber	0.1 M KHCO <sub>3</sub>	-1.6 V vs. SCE	18.8	82.1	Ling Zhao et al. <sup>[20]</sup>
Sn-pNWs	0.1 M KHCO <sub>3</sub>	-0.8 V vs. RHE	4.8	80.1	M. Spurgeon et al. <sup>[21]</sup>
np-Sn/SnO <sub>2</sub>	0.5 M KHCO <sub>3</sub>	-1.1 V vs. RHE	12.8	80	Zhifeng Wang et al. <sup>[22]</sup>
Ag-Sn-rGO	0.5 M NaHCO <sub>3</sub>	-0.94 V vs. RHE	19.1	88.3	Jie Zhang et al. <sup>[23]</sup>
Sulfur-modulated tin	0.1 M KHCO <sub>3</sub>	-0.75 V vs. RHE	51.2	93	E. H. Sargent et al. <sup>[24]</sup>
Sn/SnS <sub>2</sub>	0.5 M NaHCO <sub>3</sub>	-0.7 V vs. RHE	11.8	84.5	D. R. MacFarlane et al. <sup>[25]</sup>
m-SnO <sub>2</sub>	0.1 M KHCO <sub>3</sub>	-1.15 V vs. RHE	8.12	75.2	Rose Amal et al. <sup>[26]</sup>
SnO <sub>2</sub> microsphere /GDE	0.5 M KHCO <sub>3</sub>	-1.3 V vs. RHE	7.75	62	Yuyu Liu et al. <sup>[27]</sup>
Tin modified N-doped CNFs	0.1 M KHCO <sub>3</sub>	-0.8 V vs. RHE	6.82	62	Caiyun Wang et al. <sup>[28]</sup>
SnO <sub>2</sub> (111)	0.1 M KHCO <sub>3</sub> in H-cell	-1.05-1.45 V vs. RHE	17.1 (-1.25 V vs. RHE)	83.2 (average)	<b>This work</b>
SnO <sub>2</sub> (111)	3.5 wt. % NaCl	-1.15 V vs.	~18	~95	<b>This work</b>

	in H-cell	RHE			
SnO <sub>2</sub> (111)	1 M KHCO <sub>3</sub> in flow cell	-1.3 V vs. RHE	~200	82	<b>This work</b>
SnO <sub>2</sub> (111)	1 M KOH in flow cell	-1.4 V vs. RHE	526	87.8	<b>This work</b>

---

## References

- [1] J.-H. Guo, W.-Y. Sun, *Appl. Catal. B-Environ.* **2020**, 275.
- [2] G. Kresse, J. Furthmuller, J. Hafner, *Phys. Rev. B Condens. Matter.* **1994**, 50, 13181-13185.
- [3] P. E. Blochl, *Phys. Rev. B Condens. Matter.* **1994**, 50, 17953-17979.
- [4] J. P. Perdew, K. Burke, M. Ernzerhof, *Phys. Rev. Lett.* **1996**, 77, 3865-3868.
- [5] K. Mathew, R. Sundararaman, K. Letchworth-Weaver, T. A. Arias, R. G. Hennig, *J. Chem. Phys.* **2014**, 140, 084106.
- [6] V. Barone, *J. Chem. Phys.* **2004**, 120, 3059-3065.
- [7] J. K. Nørskov, J. Rossmeisl, A. Logadottir, L. Lindqvist, *J. Phys. Chem. B* **2004**, 108, 17886-17892.
- [8] W. Luc, C. Collins, S. Wang, H. Xin, K. He, Y. Kang, F. Jiao, *J. Am. Chem. Soc.* **2017**, 139, 1885-1893.
- [9] Y. Chen, M. W. Kanan, *J. Am. Chem. Soc.* **2012**, 134, 1986-1989.
- [10] H. Won da, C. H. Choi, J. Chung, M. W. Chung, E. H. Kim, S. I. Woo, *ChemSusChem* **2015**, 8, 3092-3098.
- [11] J. Gu, F. Heroguel, J. Luterbacher, X. Hu, *Angew. Chem. Int. Ed.* **2018**, 57, 2943-2947.
- [12] L. Fan, Z. Xia, M. Xu, Y. Lu, Z. Li, *Adv. Func. Mater.* **2018**, 28.
- [13] S. Y. Choi, S. K. Jeong, H. J. Kim, I.-H. Baek, K. T. Park, *ACS Sustain. Chem. Eng.* **2015**, 4, 1311-1318.
- [14] W. Deng, L. Zhang, L. Li, S. Chen, C. Hu, Z. J. Zhao, T. Wang, J. Gong, *J. Am. Chem. Soc.* **2019**, 141, 2911-2915.
- [15] X. Zu, X. Li, W. Liu, Y. Sun, J. Xu, T. Yao, W. Yan, S. Gao, C. Wang, S. Wei, Y. Xie, *Adv. Mater.* **2019**, 31, e1808135.
- [16] S. Liu, J. Xiao, X. F. Lu, J. Wang, X. Wang, X. W. D. Lou, *Angew. Chem. Int. Ed.* **2019**, 58, 8499-8503.
- [17] X. Bai, W. Chen, C. Zhao, S. Li, Y. Song, R. Ge, W. Wei, Y. Sun, *Angew. Chem. Int. Ed.* **2017**, 56, 12219-12223.
- [18] F. Li, L. Chen, G. P. Knowles, D. R. MacFarlane, J. Zhang, *Angew. Chem. Int. Ed.* **2017**, 56, 505-509.
- [19] F. Lei, W. Liu, Y. Sun, J. Xu, K. Liu, L. Liang, T. Yao, B. Pan, S. Wei, Y. Xie, *Nat. Commun.* **2016**, 7, 1-8.
- [20] H. Hu, L. Gui, W. Zhou, J. Sun, J. Xu, Q. Wang, B. He, L. Zhao, *Electrochim. Acta* **2018**, 285, 70-77.

- [21]B. Kumar, V. Atla, J. P. Brian, S. Kumari, T. Q. Nguyen, M. Sunkara, J. M. Spurgeon, *Angew. Chem. Int. Ed.* **2017**, *56*, 3645-3649.
- [22]S. Liu, F. Pang, Q. Zhang, R. Guo, Z. Wang, Y. Wang, W. Zhang, J. Ou, *Appl. Mater. Today* **2018**, *13*, 135-143.
- [23]X. Zhang, F. Li, Y. Zhang, Alan M. Bond, J. Zhang, *J. Mater. Chem. A* **2018**, *6*, 7851-7858.
- [24]X. Zheng, P. De Luna, F. P. García de Arquer, B. Zhang, N. Becknell, M. B. Ross, Y. Li, M. N. Banis, Y. Li, M. Liu, O. Voznyy, C. T. Dinh, T. Zhuang, P. Stadler, Y. Cui, X. Du, P. Yang, E. H. Sargent, *Joule* **2017**, *1*, 794-805.
- [25]F. Li, L. Chen, M. Xue, T. Williams, Y. Zhang, D. R. MacFarlane, J. Zhang, *Nano Energy* **2017**, *31*, 270-277.
- [26]R. Daiyan, X. Lu, W. H. Saputera, Y. H. Ng, R. Amal, *ACS Sustain. Chem. Eng.* **2018**, *6*, 1670-1679.
- [27]Y. Fu, Y. Li, X. Zhang, Y. Liu, J. Qiao, J. Zhang, D. P. Wilkinson, *Appl. Energy* **2016**, *175*, 536-544.
- [28]Y. Zhao, J. Liang, C. Wang, J. Ma, G. G. Wallace, *Adv. Energy Mater.* **2018**, *8*, 1702524.